

High-Sensitivity CMOS Super-Regenerative Receiver with Quench-Controlled High- Q Metamaterial Resonator for Millimeter-Wave Imaging at 96 and 135 GHz

Yang Shang, *Student Member, IEEE*, Hao Yu, *Senior Member, IEEE*, Sanming Hu, *Senior Member, IEEE*, Yuan Liang, Xiaojun Bi, and Muthukumaraswamy Annamalai Arasu

Abstract—High-sensitivity super-regenerative receivers (SRXs) are demonstrated at 96 and 135 GHz, respectively, in this paper. They are based on high- Q quench-controlled metamaterial resonators with a differential transmission line loaded with a split-ring resonator (DTL-SRR) and a differential transmission line loaded with a complementary split-ring resonator (DTL-CSRR) in 65-nm CMOS. High- Q oscillatory amplifications are established by the sharp stopband introduced by metamaterial resonators. As such, high detection sensitivity is achieved for SRXs at millimeter-wave regions. The fabricated 96-GHz DTL-CSRR-based SRX has a compact core chip area of 0.014 mm^2 with measured power consumption of 2.8 mW, sensitivity of -79 dBm , noise figure (NF) of 8.5 dB, and noise equivalent power (NEP) of $0.67 \text{ fW}/\sqrt{\text{Hz}}$. The fabricated 135-GHz DTL-SRR-based SRX has a compact core chip area of 0.0085 mm^2 with measured power consumption of 6.2 mW, sensitivity of -76.8 dBm , NF of 9.7 dB, and NEP of $0.9 \text{ fW}/\sqrt{\text{Hz}}$. Compared to the conventional SRX with an LC-tank-based resonator at similar frequencies, the proposed SRXs have $2.8\sim 4 \text{ dB}$ sensitivity improvement and 60% smaller area. The integrated SRXs are also demonstrated for the imaging applications.

Index Terms—Imaging, metamaterial resonator, 65-nm CMOS, super-regenerative receiver (SRX).

I. INTRODUCTION

MILLIMETER-WAVE radiation above 100 GHz has a moderate wavelength that not only allows penetration into nonconductive materials with nonionizing nature, but also has high spatial resolution. It shows great potential for noninvasive imaging applications in various areas such as pharmacy and security [1]–[5]. With the recent advance of CMOS technology, CMOS-based millimeter-wave (60–300 GHz) signal

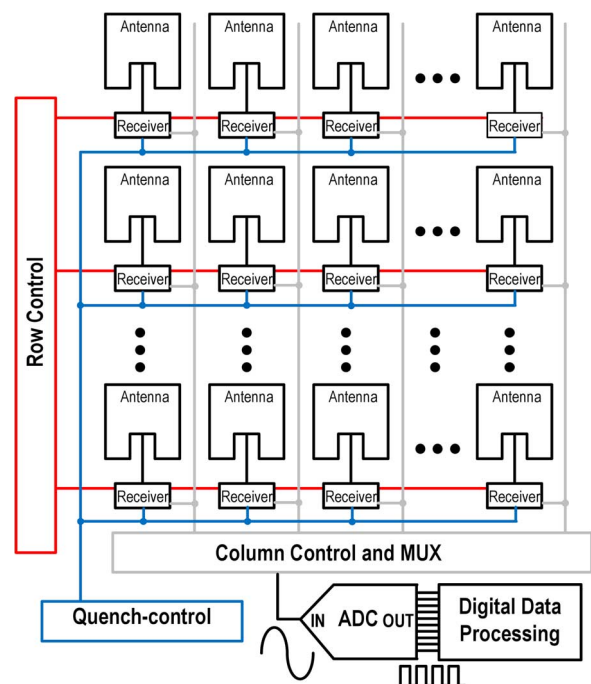


Fig. 1. Large-arrayed CMOS millimeter-wave imaging system.

transmitting and receiving components have been recently developed [6]–[11]. Similarly, one can thereby develop a low-cost, portable, and large-arrayed millimeter-wave imaging system in CMOS, as illustrated in Fig. 1, where each millimeter-wave image pixel consists of a receiver and an antenna. However, the signal strength of millimeter-wave radiation above 100 GHz is usually weak when generated by CMOS, and great path loss will be introduced by absorption and diffraction during the propagation. As such, it is challenging to design a high-sensitivity receiver to generate sufficient margin in the link budget. Moreover, a large-arrayed receiver is desired to improve both spatial resolution and image capturing speed, which requires a compact design of each millimeter-wave image pixel.

The recent super-regenerative receiver (SRX) [12] can achieve high sensitivity within narrow band, which is optimum for millimeter-wave imaging [8], [13] that has a relative low data rate. Note that even though the data rate of the SRX is usually limited by the bandwidth, it is still more than enough

Manuscript received April 02, 2014; revised August 01, 2014; accepted September 07, 2014. Date of publication October 15, 2014; date of current version December 02, 2014. This work was supported by the Singapore MOE Tier-1 funding under Grant RG 26/10 and under Grant NRF2010NRF-POC001-001. This paper is an expanded version from the IEEE Radio Frequency Integrated Circuits Symposium, June 2, 2013.

Y. Shang, H. Yu, and Y. Liang are with the School of Electrical and Electronic Engineering, Nanyang Technological University, Singapore 639798 (e-mail: haoyu@ntu.edu.sg).

S. Hu is with the Institute of Microwave Techniques, University of Ulm, Ulm 89081, Germany.

X. Bi and M. A. Arasu are with the Institute of Microelectronics, Agency for Science, Technology and Research (A*STAR), Singapore 117685.

Color versions of one or more of the figures in this paper are available online at <http://ieeexplore.ieee.org>.

Digital Object Identifier 10.1109/TMTT.2014.2360677

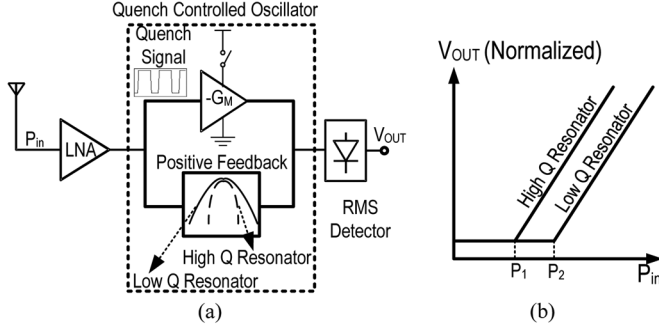


Fig. 2. (a) Block diagram of SRX. (b) Impact of resonator Q -factor to receiver sensitivity.

to carry a VGA video stream. As depicted in Fig. 2(a), the core of the SRX is a quench-controlled oscillator, which consists of a resonator with positive feedback to realize an oscillatory amplification. When a periodic quench-control signal is applied, the average of the detected signal envelope is amplified for the injected RF signal from the low-noise amplifier (LNA). Although an LNA stage with high gain can help improve the receiver responsivity and sensitivity, it has to be implemented with a much larger chip area and power consumption when compared to the SRX design. Note that the available power gain of a typical nMOS transistor in 65-nm CMOS is approaching unity at 150 GHz. Therefore, the LNA is replaced by a common source buffering stage for the isolation above 100 GHz in the SRX design. As illustrated in Fig. 2(b), one compact and high-sensitivity SRX for an millimeter-wave imaging system requires a compact and high quality factor (Q) resonator. Note that V_{OUT} is a normalized voltage of the root mean square (rms) detector. However, the Q of the traditional LC -tank-based resonator [14]–[16] has significant performance degradation with a large area at the millimeter-wave region.

Recently, metamaterial-based resonators have been explored in [17]–[19] to improve the Q with a compact area at the millimeter-wave region. A split-ring resonator (SRR) or a complementary split-ring resonator (CSRR) can be designed in the CMOS process to provide negative permeability (μ) or negative permittivity (ϵ) for millimeter-wave wave propagation, respectively. When loading the SRR or CSRR to a host transmission line (TL-SRR and TL-CSRR), the integrated structure becomes a nontransmission medium with single-negative property ($\mu \cdot \epsilon < 0$) in the vicinity of resonance frequency. A sharp stopband is thereby formed to perfectly reflect the incident millimeter-wave at the SRR or CSRR loading point with a stable standing wave established in the host T-line [17]–[19]. Compared to the traditional LC -tank-based resonator, the TL-SRR and TL-CSRR have stable electromagnetic (EM) energy storage within a compact area, which result in a much higher Q . As such, it becomes relevant to study the CMOS on-chip SRR or CSRR for the compact and high-sensitivity SRX design in a millimeter-wave imaging system. As demonstrated in this paper, two SRXs with quench-controlled high- Q metamaterial resonators, differential T-line loaded with a complementary split-ring resonator (DTL-CSRR) and differential T-line loaded with a split-ring resonator (DTL-SRR) have much higher sensitivity as well as a smaller area than

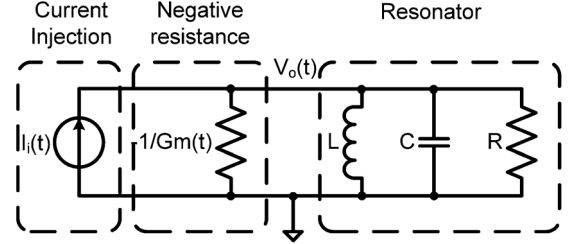


Fig. 3. Simplified equivalent-circuit model of super-regenerative amplifier.

the traditional LC -tank-based designs [8], [13]. In addition, an integrated 135-GHz imager has been demonstrated with various pharmacy and security imaging applications. The remainder of this paper is organized as follows. The fundamentals of SRA are first reviewed in Section II, and the design of the quench-controlled oscillator by metamaterial resonators is discussed in Section III. Section IV introduces the CMOS SRX designs at 96 and 135 GHz, respectively. The measurement results are presented in Section V with a conclusion in Section VI.

II. FUNDAMENTALS OF SRA

Generally, an SRX consists of a quench-controlled oscillator injected by an external signal and an envelope detector. The process of injecting external signal into a quench-controlled oscillator is firstly reviewed to understand the operation of the SRX, called super-regenerative amplification (SRA).

A. Equivalent Circuit of SRA

A simplified circuit model of SRA is shown in Fig. 3. The resonator is modeled by an RLC block, and its oscillation is quench controlled by a time-dependent negative resistance $-1/G_m(t)$, where G_m is the equivalent conductance determined by the associated active devices. The external signal injected is modeled as a time-dependent current source $I_i(t)$. $V_o(t)$ is the output voltage. The resonance frequency is $\omega_0 = 1/\sqrt{LC}$; the quality factor is $Q_0 = R/Z_0 = 0.5\zeta_0^{-1}$; Z_0 and ζ_0 are the characteristic impedance and quiescent damping factor, respectively.

Assuming $G_m(t)$ varies much slower than ω_0 such that a quasi-static condition holds in the system to have a time-varying transfer function in the s -domain by

$$\frac{V_o(s, t)}{I_i(s)} = \frac{Z_0 \omega_0 s}{s^2 + 2\zeta(t)\omega_0 s + \omega_0^2} \quad (1)$$

where $\zeta(t) = \zeta_0[1 - G_m(t)R]$ is the instantaneous damping factor.

A second-order linear time variant system can be observed from (1). By varying $\zeta(t)$, the pole can be shifted between left and right sides of the s -plane periodically. In other words, the oscillation starts in SRA when $\zeta(t)$ is negative, and stops when $\zeta(t)$ is positive. Note that (1) is only valid when SRA works in the linear mode such that $V_o(s, t)$ is small enough to prevent significant distortion in each quench cycle. Generally, SRA working in the linear mode is preferred in the application of millimeter-wave imaging since it has a better sensitivity than that in the logarithmic mode [20], [21].

After Laplace transform, (1) can be written as a second-order differential equation in time domain

$$v_o''(t) + 2\zeta(t)\omega_0 v_o'(t) + \omega_0^2 v_o(t) = Z_0\omega_0 I_i'(t) \quad (2)$$

assuming the oscillation is fully quenched in each cycle, such that $v_o(t)$ is independent of the previous ones. For a particular quench cycle $t \in (t_a, t_b]$ with $t_a < 0 < t_b$, if $\zeta(t)$ is positive for $t \in (t_a, 0]$ and negative for $t \in (0, t_b]$, (2) can be written as [21]

$$v_o(t) = \frac{Z_0}{s(t)} \int_{t_a}^t I_i'(\tau) s(\tau) \sin[\omega_0(t - \tau)] d\tau \quad (3)$$

where $s(t) = e^{\omega_0 \int_0^t \zeta(\lambda) d\lambda}$ is called the sensitivity function, and it reaches maximum when $t = 0$; and decays rapidly with t . As a result, the SRA is only sensitive to the input $I_i'(t)$ in the time window centered at $t = 0$ when $\zeta(t)$ turns from positive to negative.

B. Frequency Response of SRA

The frequency response of SRA can be analyzed with a convolution model [22]. For a ac input with $I_i(t) = I_0 \sin(\omega_i t + \phi_i)$, the output waveform can be approximated by

$$v_o(t) \approx \frac{Z_0\omega_i I_0}{2s(t)} |S(\Delta\omega)| \sin(\omega_0 t + \phi_i) \quad (4)$$

where $\Delta\omega = \omega_0 - \omega_i$ and $S(\omega)$ is the Fourier transform of $s(t)$. In the application of millimeter-wave imaging, we are more interested in the envelope of v_o , which is

$$\text{Env}[v_o(t)] = \frac{Z_0\omega_i I_0}{2s(t)} |S(\Delta\omega)|. \quad (5)$$

Assuming ω_i is very close to ω_0 ($\Delta\omega \ll \omega_i$), a quasi-static condition holds in (5) that the frequency response of $\text{Env}(v_o(t))$ is determined by $|S(\Delta\omega)|$.

For a typical ramping quench signal with time variant conductance $G_m = (1/R)(kt + 1)$, where k is the normalized ramping slope of G_m with the unit of $1/s$, the instantaneous damping factor is $\zeta(t) = -(k/2Q_0)t$. Thus, the envelope of $v_o(t)$ can be solved by

$$\text{Env}[v_o(t)]_{\text{ramp}} = \frac{\sqrt{\pi} Z_0\omega_i I_0}{\Omega_0} e^{\frac{\Omega_0^2}{4} t^2} e^{-\frac{\Delta\omega^2}{\Omega_0^2}} \quad (6)$$

where $\Omega_0 = \sqrt{k\omega_0/Q_0}$ is a constant that determines the frequency response of SRA, e.g., the 3-dB bandwidth of SRA equals $1.177 \Omega_0$. As such, one can observe that for the given k and ω_0 , the bandwidth is inversely proportional to Q_0 .

C. Sensitivity of SRA

The sensitivity of SRA is defined as the minimum detected power that means the induced output signal power is the same as its variance

$$S_{\text{SRA}} = P_{\min}|_{I_x^2 = \sigma_x^2} = \frac{I_0^2 R}{2} \Big|_{I_x^2 = \sigma_x^2} \quad (7)$$

where I_x is the equivalent induced in SRA in response to the ac input I_i , and σ_x^2 is the variance of I_x .

As discussed in [22], for a typical ramp-damping function with a normalized ramping slope of k , we have

$$I_x = \frac{I_0\omega_0\sigma_s}{2} \quad \sigma_x^2 = \frac{N\omega_0^2 E_g}{2} \quad (8)$$

where $\sigma_s = \sqrt{2Q_0/\omega_0 k}$ is the SRA time constant with a unit of $s/\sqrt{\text{rad}}$, $E_g = \sigma_s \sqrt{\pi}$ is the energy of density function, and N is the noise power density with $N = 4K \cdot T \cdot F/R$. Note that K and F denote the Boltzmann constant and noise factor of SRA contributed by active devices, respectively.

As such, the sensitivity of the SRX can be found by substituting (8) into (7)

$$S = 2KTF \sqrt{\frac{k\omega_0}{\pi Q_0}}. \quad (9)$$

Note that the receiver noise figure (NF) can be approximated as [8]

$$\text{NF} = \frac{S}{K \cdot T \cdot B}. \quad (10)$$

Note that the NF of an SRX is independent of the quench signal. For a typical 3-dB bandwidth of the SRX ($B = 1.177 \Omega_0$), the NF becomes 0.958 F. In addition, the noise equivalent power (NEP) can be calculated by S/\sqrt{B}

$$\text{NEP} = 1.38KTF \sqrt[4]{\frac{k\omega_0}{\pi Q_0}}. \quad (11)$$

Note that k is usually determined by the frequency of the quench signal and the sampling rate of one SRA. Therefore, it can be observed from (9) and (11) that, for a given ω_0 and k , the sensitivity and NEP are inversely proportional to the square-root and the fourth root of Q_0 , respectively.

Thus, the resonator with higher Q will significantly improve the sensitivity within the interested bandwidth for imaging application.

D. Millimeter-Wave Imaging by SRA Detection

Millimeter-wave radiation is usually attenuated due to absorption and scattering during the propagation [23], which can be modeled by

$$I_{\gamma_1} = I_{\gamma_0} e^{-\int_{\gamma_0}^{\gamma_1} \alpha_e(z) dz} \quad (12)$$

where I_{γ_0} and I_{γ_1} are the incoming and outgoing radiance intensity along path (γ_0, γ_1) ; and $\alpha_e(z)$ is the extinction coefficient, which is the summation of absorption (α_a) and scattering (α_s) coefficients. For a homogeneous material placed between (γ_0, γ_1) , α_a is a constant. The scattering only happens at the interface with scattering coefficients of $\alpha_s(\gamma_0)$ and $\alpha_s(\gamma_1)$. The received power (P_R) in a transmission-type millimeter-wave imaging system is [24]

$$P_R \text{ (dBm)} = P_T \text{ (dBm)} + G_R \text{ (dBi)} - L \text{ (dB)} - 8.686 [\Delta\gamma\alpha_a + \alpha_s(\gamma_0) + \alpha_s(\gamma_1)] \text{ (dB)} \quad (13)$$

where P_T is the effective isotropic radiated power (EIRP) of the transmitter, G_R is the receiver antenna gain, and L is the path loss without any objects placed in the propagation path, including both the free-space path loss (FSPL) and atmosphere absorption.

As shown in (5), the envelope of receiver output is proportional to the injected ac or the square-root of input power. A dc output can be obtained by averaging $\text{Env}[v_o(t)]$ in each periodic quenching cycle

$$V_{DC} = \frac{\omega_i Z_0 |S(\Delta\omega)| \sqrt{P_R}}{\sqrt{2R}(t_b - t_a)} \int_0^{t_b} \frac{1}{s(t)} dt. \quad (14)$$

As such, the received power could be detected by measuring V_{DC} from the SRA output. As a result, the millimeter-wave image of an object can be further obtained by the 2-D scanning of V_{DC} with fixed P_T , G_R , and L . Moreover, by analyzing V_{DC} as well as P_R with various object thickness ($\Delta\gamma$), one can further find the absorption coefficient of the object under test.

III. QUENCH-CONTROLLED OSCILLATOR BY METAMATERIAL RESONATOR

As discussed in Section II, a high- Q resonator is needed in the quench-controlled oscillator to improve the sensitivity of the SRX at the millimeter-wave region. In this section, the design of the high- Q on-chip metamaterial resonator will be discussed followed by the design of quench-controlled oscillator.

A. On-Chip Metamaterial Resonators

Metamaterial with a negative refraction index was first demonstrated in 2001 with SRRs showing $\mu < 0$ at resonance frequency [25]. A planar SRR structure can be considered as a magnetic dipole excited by the magnetic field (H -field) along the ring axis. A CSRR was proposed [26] as a dual counterpart of the SRR with $\varepsilon < 0$ at resonance frequency. A planar CSRR structure can be considered as an electric dipole excited by the electric field (E -field) along the ring axis. Since the feature size of the passive device is inversely proportional to the operation frequency, the size of the SRR or CSRR will thereby become more compact for on-chip implementation in the millimeter-wave region. As explored in the millimeter-wave region, both the SRR and CSRR can be applied as the load for a T-line to build compact on-chip metamaterial resonators with a high- Q factor [19].

An electric or magnetic plasmonic medium with single negative ε or μ could be formed when coupling either the SRR or CSRR as the load to a host T-line, respectively. There is a sharp bandgap or stopband in such a medium at the resonant frequency such that the EM wave can be perfectly reflected back into the host T-line to form a stable standing wave. Ideally, the EM energy is stored into the compact SRR or CSRR structure, where the energy density can be significantly increased with a high- Q factor.

1) *T-Line Loaded With SRR*: T-line loaded with SRR (TL-SRR) can be implemented on chip by the top most metal layer, as shown in Fig. 4(a). A magnetic plasmonic medium is formed in the vicinity of SRR resonance frequency by exciting the SRR with the magnetic flux generated from the differential ac in the

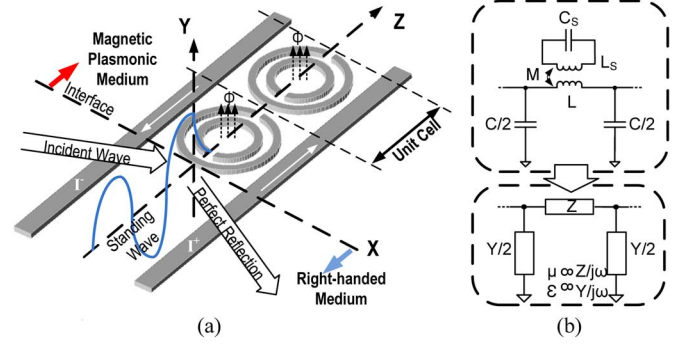


Fig. 4. (a) Standing wave formed by perfect reflection at DTL-SRR load. (b) Equivalent circuit of DTL-SRR with metamaterial condition to form perfect reflection.

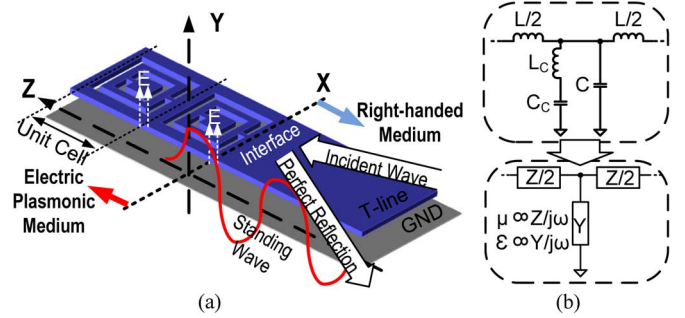


Fig. 5. (a) Standing-wave formed by perfect reflection at DTL-CSRR load. (b) Equivalent circuit of DTL-CSRR with metamaterial condition to form perfect reflection.

host T-line. The equivalent circuit of TL-SRR unit-cell is depicted in Fig. 4(b), where L and C are the intrinsic series inductance and shunt capacitance of the T-line, L_s and C_s are the equivalent inductance and capacitance of the SRR, and M is the mutual inductance between the SRR and T-line.

The metamaterial property for the TL-SRR can be analyzed by the T-line model [27] with distributed series impedance (Z) and shunt admittance (Y), which are determined by ε and μ , respectively. It can be shown that the $\varepsilon > 0$ and $\mu < 0$ condition is satisfied by the TL-SRR in the frequency range $\sqrt{1/L'_s C'_s} < \omega < \sqrt{(L + L'_s)/LL'_s C'_s}$, where $L'_s = C_s M^2 \omega^2$ and $C'_s = L_s/(M^2 \omega^2)$ are the equivalent series inductance and capacitance of the SRR [19]. Note that M needs to be sufficiently high for a negative μ . As such, a differential host T-line is deployed in the design with SRRs placed in between as close as possible.

2) *T-Line Loaded With CSRR*: What is more, a T-line loaded with a CSRR (TL-CSRR) can be implemented on chip by engraving CSRRs on the T-line in the top most metal layer, as shown in Fig. 5(a). An electric plasmonic medium is formed by exciting the CSRR with the E -field in the host T-line in the vicinity of CSRR resonance frequency. The equivalent circuit of the TL-CSRR unit-cell is depicted in Fig. 5(b), where L_C and C_C are the equivalent inductance and capacitance of the CSRR resonator. Comparing the equivalent circuit of the TL-CSRR unit-cell with the one of the T-line unit-cells, one can observe the evanescent wave condition ($\varepsilon < 0$ and $\mu > 0$) is satisfied in the TL-CSRR in the frequency range $\sqrt{1/C_C L_C} < \omega < \sqrt{C + C_C/CC_C L_C}$.

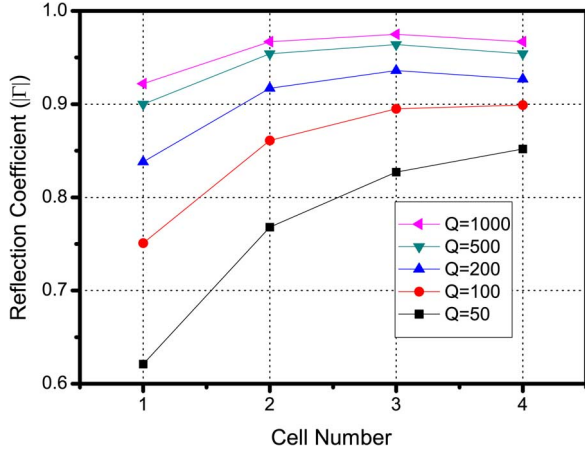


Fig. 6. Reflection coefficient of T-line loaded with CSRR unit-cells.

B. Quench-Controlled Oscillation

1) *High- Q Resonance With Standing Wave*: In the practical on-chip resonator design with a finite Q of the SRR or CSRR, the reflection coefficient ($|\Gamma|$) depends on the number of cascading TL-SRR or TL-CSRR unit-cells. Fig. 6 shows the circuit-level simulation of the TL-CSRR at 96-GHz resonance frequency with the following observations. First, the reflection coefficient $|\Gamma|$ is more sensitive to the cells number when Q is below 200. Second, $|\Gamma|$ can be improved by cascading more unit-cells.

2) *Voltage-Controlled Negative Resistance*: The oscillation can be sustained by compensating the reflection loss ($|\Gamma| < 1$) with a negative resistance. Similarly, a quench-controlled oscillating can be achieved by controlling voltage-controlled negative resistance (VCNR), which determines the instantaneous damping factor ($\zeta(t)$) of (1) as discussed in Section II. The sensitivity of the SRX is also a function of $\zeta(t)$ that is determined by VCNR. Usually a cross-coupled nMOS pair is applied for the differential negative resistance design, as depicted in Fig. 7, where the tail dc of the cross-coupled nMOS pair (I_D) can be quench controlled by another nMOS biased in the saturation region. The equivalent differential negative conductance between nodes “a” and “b” can be expressed as below by neglecting the channel-length modulation

$$G_m = \frac{gm_2}{2} = \frac{I_D}{2V_{od2}} \quad (15)$$

where gm_2 and V_{od2} are the transconductance and overdrive voltage of cross-coupled nMOS field-effect transistors (FETs), respectively. Note that I_D can be obtained by

$$I_D = \frac{W_1}{2L_1} \mu_n C_{ox} V_{od1}^2 = \frac{W_2}{L_2} \mu_n C_{ox} V_{od2}^2 \quad (16)$$

where W_1 , L_1 , and $V_{od1} = V_Q - V_T$ are the channel width, length, and overdrive voltage of the tail NMOS; W_2 , L_2 , and V_{od2} are the channel width, length, and overdrive voltage of the cross-coupled nMOS pair; and $\mu_n C_{ox}$ and V_T are the process-

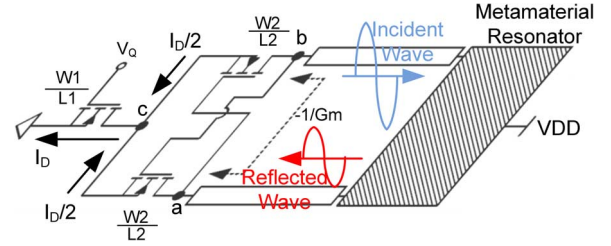


Fig. 7. Reflection loss compensation by cross-coupled nMOS pair with controlled tail dc.

related parameters. As such, (15) can be written as a function of V_Q by

$$G_m = \frac{\mu_n C_{ox} (V_Q - V_T)}{4} \sqrt{\frac{2W_1 W_2}{L_1 L_2}}. \quad (17)$$

One can observe from (17) that G_m is linearly controlled by V_Q of which the slope is determined by the product of W_1/L_1 and W_2/L_2 . Note that the oscillation starts when $1/G_m < R$ and stops when $1/G_m > R$. As such, $(W_1/L_1)(W_2/L_2)$ must be large enough to satisfy the oscillation start condition ($1/G_m < R$). However, large W_2/L_2 will introduce additional parasitic capacitance, which will be counted into the resonator rank and reduce the oscillation frequency. Moreover, in order to provide sufficient head room for the cross-coupled nMOS pair, W_1/L_1 is selected several times larger than W_2/L_2 .

IV. SRX DESIGN BY METAMATERIAL RESONATOR

In order to demonstrate the advantages of the metamaterial resonator based SRX, two SRXs working at 96 and 135 GHz are implemented in the 65-nm CMOS process with TL-CSRR and TL-SRR, respectively.

A. SRX Design by TL-CSRR

1) *Folded Differential T-Line Loaded With CSRR*: The TL-CSRR structure cannot be directly employed for the SRX design. Firstly, the single-ended approach will bring large common-mode noise in the oscillator; secondly, cascading more unit-cells will increase area overhead. A folded differential T-line loaded with a CSRR (DTL-CSRR) structure is proposed to reduce the area by half while doubling the number of the unit-cell [28]. As shown in Fig. 8, two cascaded TL-CSRR unit-cells (with a CSRR size of $60 \times 60 \mu\text{m}^2$) are folded in the two top most metal layers (M6 and M7).

The S -parameters of the proposed DTL-CSRR structure is verified by the EM simulation tool EMX with a parasitic capacitance of 40 fF from transistors. Both ϵ and μ of the DTL-CSRR are extracted from the simulation results according to the procedure in [29], which become both complex numbers due to the existence of loss factor induced imaginary parts. The metamaterial property is illustrated by the real parts of ϵ and μ in Fig. 9. At the vicinity of 105-GHz resonance frequency, an electric plasmonic medium is formed with $\epsilon < 0$ and $\mu > 0$. A stopband is thereby formed within a narrow bandwidth of 1.8 GHz, where

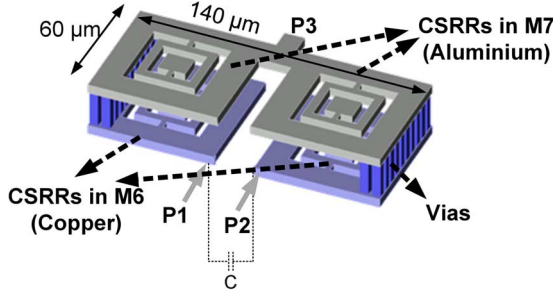


Fig. 8. Layout for CMOS on-chip implementation of DTL-CSRR for 96-GHz SRX.

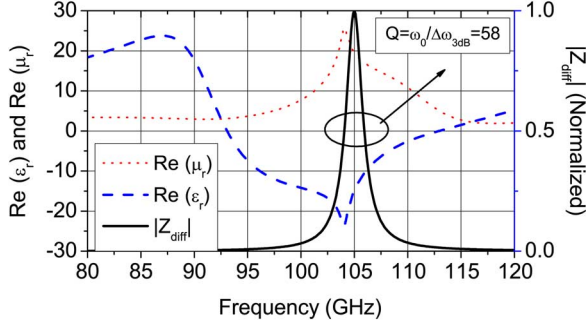


Fig. 9. EM-simulation based comparison of DTL-CSRR and LC-tank resonator for CMOS 96-GHz SRX design.

the Q factor is found to be 58 by $Q = \omega_0 / \omega_{3\text{dB}}$ dB from the differential impedance (Z_{diff}) between P1 and P2.

2) *96-GHz DTL-CSRR-Based SRX*: Fig. 10 depicts the schematic of the DTL-CSRR-based SRX. The DTL-CSRR is firstly connected to a differential negative resistance formed by cross-coupled nMOS (M2 and M3). To further improve the detection efficiency, a virtual ground at 96 GHz is formed by two $\lambda/4$ stubs. The size of M4 is designed as four times of M2 and M3. Note that W_{Total} and W_{Single} are the total and individual finger width of transistors in Fig. 10, respectively. The channel length of every active device is 60 nm. The remaining circuit consists of a common source input buffer (M1) for ac injection and an envelope detector formed by M5 and M6. The common source stage (M1) is designed for input signal injection and also reverse isolation from the oscillator to the input. The size of M1 is optimized with consideration of minimized parasitic capacitance as well as the input matching. Similarly, M5 and M6 also need to be minimized, but doing so will reduce the detection efficiency. To solve this problem, a capacitance coupling by C1 and C2 is introduced between the outputs of the oscillator tank and envelope detection. Firstly, the capacitance loading from M5 and M6 are reduced by series connection of the coupling capacitors; Secondly, M5 and M6 are biased externally by large resistors (R1, R2) to optimize the detection; thirdly, $1/f$ noise from M5 and M6 is also isolated. Note that a tradeoff is required to the values of C1 and C2, as the detection responsivity will be reduced due to a partially voltage transfer by the capacitance coupling.

B. SRX Design by TL-SRR

1) *Differential T-Line Loaded With SRR*: The TL-SRR structure with horizontal placement of SRRs (Fig. 4) is also not

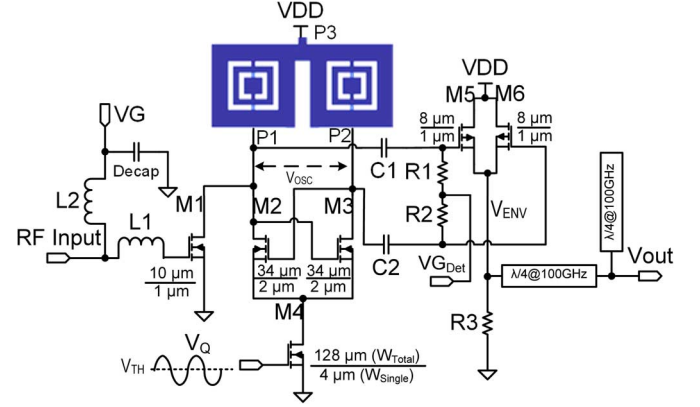


Fig. 10. Schematic of CMOS 96-GHz SRX with DTL-CSRR.

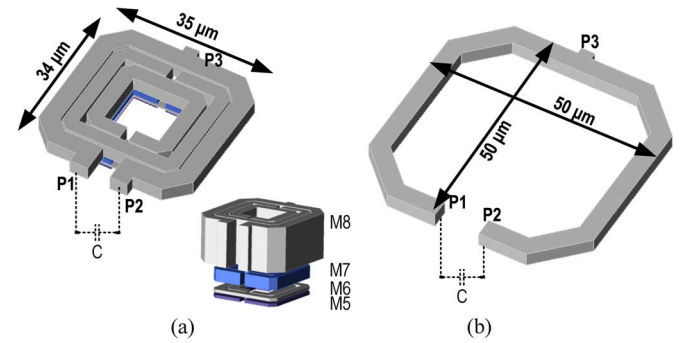


Fig. 11. Layout for CMOS on-chip implementation of DTL-SRR for 135-GHz SRX.

suitable for the practical implementation for the SRX, mainly due to the large area overhead. Compared to the TL-CSRR, the TL-SRR inherently has better layout flexibility because SRRs can be vertically stacked within a compact area. One differential T-line loaded with stacked SRRs (DTL-SRR) is proposed in this work for the application of 135-GHz SRX design in the 65-nm CMOS RF process.

As shown in Fig. 11(a), the DTL-SRR is designed by stacked SRRs with the same dimensions of $24 \times 24 \mu\text{m}^2$ in four metal layers (M5 to M8). All SRRs are closely coupled to the same host T-line implemented in the top most metal layer (M8). The overall size of the proposed DTL-SRR is $35 \times 34 \mu\text{m}^2$. For the purpose of comparison, a traditional LC-tank resonator is designed in the M8 metal layer, as shown in Fig. 11(b), which has the same resonance frequency of 135 GHz. The S-parameters of both structures are also verified by EMX with the same parasitic capacitance of 18 fF. As shown in Fig. 12, at the vicinity of 140-GHz resonance, $\epsilon > 0$ and $\mu < 0$, and a magnetic plasmonic medium is formed. As a result, a stopband is formed at 140 GHz within a narrow bandwidth of 3.5 GHz. The Q factor of the DTL-SRR resonator is 40, which is more than two times of the Q of the LC-tank resonator. Moreover, the DTL-SRR resonator layout area ($1190 \mu\text{m}^2$) is less than half of the LC-tank resonator ($2500 \mu\text{m}^2$).

2) *135-GHz DTL-SRR-Based SRX*: Fig. 13 depicts the schematic of a 135-GHz DTL-SRR-based SRX. Firstly, a transformer based matching network is applied to the input

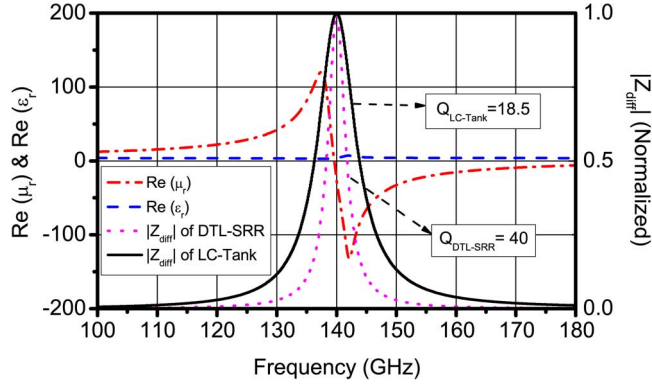


Fig. 12. EM-simulation based comparison of DTL-SRR and LC-tank resonator for CMOS 135-GHz SRX design.

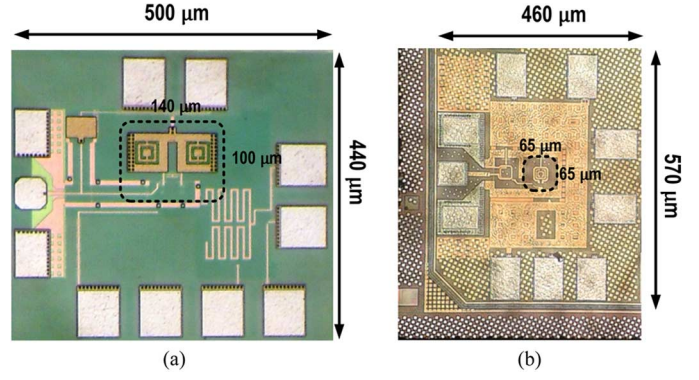


Fig. 14. Die micrographs. (a) CMOS 96-GHz SRX with DTL-CSRR. (b) CMOS 135-GHz SRX with DTL-SRR.

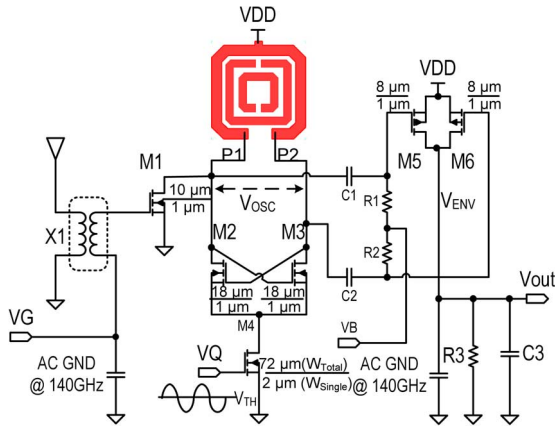


Fig. 13. Schematic of CMOS 135-GHz SRX with DTL-SRR.

matching for M1 for the electrostatic discharge (ESD) protection when integrating with the antenna; secondly, the virtual ground formed by two $\lambda/4$ T-lines is replaced by the high- Q metal-oxide-metal (MOM) capacitor to further reduce the chip area; thirdly, the detected envelope signal V_{ENV} is directly averaged by an on-chip low-pass filter formed by R3 and C3 at the output.

V. MEASUREMENT RESULTS

A. DTL-CSRR-Based SRX at 96 GHz

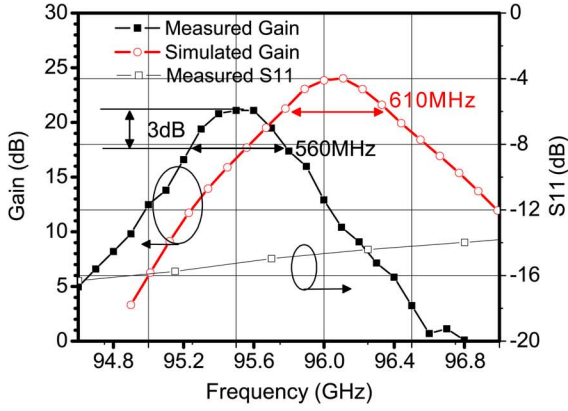
The chip micrograph of the proposed DTL-CSRR-based SRX is shown in Fig. 14(a). It is fabricated in a 65-nm CMOS process with a total die area of $500 \times 440 \mu\text{m}^2$, and a core area of 0.014 mm^2 including a resonator and active devices. The SRX is measured on a probe station (CASCADE Microtech Elite-300) with an RF input signal provided by Agilent PNA-X (N5247A) with transmit/receive (T/R) modules (N5260) of which the output power is calibrated in the range from $-85 \sim -10 \text{ dBm}$ by an Agilent Spectrum Analyzer E4407B with a W-band waveguide harmonic mixer (11970 W). Note that the output power of the T/R module can be controlled by N5247A, but its minimum output power level that can be calibrated is limited by the sensitivity of the spectrum analyzer. According to the specification of this spectrum analyzer, the accuracy of the output power level after calibration is $\pm 0.3 \text{ dB}$. A

12.5-MHz sinusoid quench-control signal is applied by a function generator (AFG3022) with voltage swept in $0 \sim 250 \text{ mV}$. The receiver operates under a 1-V power supply with a power consumption of 2.8 mW .

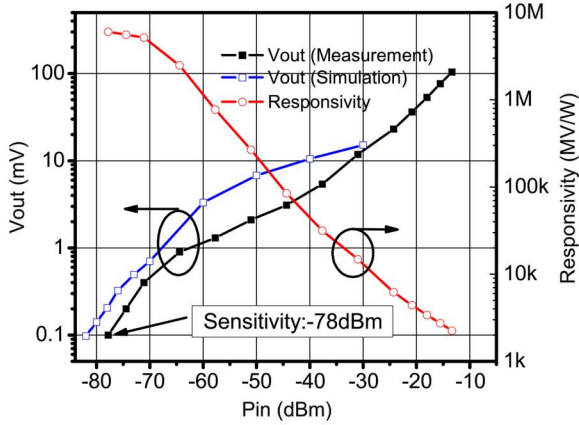
The receiver gain is defined as $\text{Gain (dB)} = 20 \log V_{out} - P_{in}$, where V_{out} is the normalized output voltage of the receiver and P_{in} is the input power level of the proposed SRX in the decibel-watt (dBW). Although the receiver gain is independent to P_{in} according to (5) in Section II, a relative higher P_{in} of -20 dBm is applied to have sufficient V_{out} at the frequency outside the bandwidth. Fig. 15(a) shows the measured gain and input S11, where the maximum gain of the proposed SRX is 21 dB at 95.5 GHz and a 3-dB bandwidth of 560 MHz is observed. The measured gain is quite close to the post-layout simulation result. A good input match is also observed with S11 smaller than -14 dB in $94.6 \sim 96.6 \text{ GHz}$. Fig. 15(b) shows the V_{out} against P_{in} as well as the responsivity at 95.5 GHz . The responsivity is defined by V_{out}/P_{in} . Almost linear responses are observed for both measurement and simulation results of V_{out} . Note that the sensitivity is observed at 0.1 mV V_{out} , which is the normalized output voltage compared to the output voltage level without any RF input. The measured sensitivity is -78 dBm at 95.5 GHz , which is 4 dB higher than the simulation result. Such a difference is probably due to the loss of the RF PAD when connected to the ground-signal-ground (GSG) probe. Moreover, a maximum responsivity of 6.02 MV/W is observed at the sensitivity level of input. As a result of the differences in both sensitivity and bandwidth between the measurement and simulation results, the calculated NEP of the proposed SRX based on measurement and simulation results are 0.67 and $0.26 \text{ fW}/\sqrt{\text{Hz}}$, respectively. Finally, the NF is found to be 8.5 dB by (10) at 95.5 GHz at room temperature of 290 K .

B. DTL-SRR-Based SRX at 135 GHz

The proposed DTL-SRR-based SRX is implemented in a 65-nm CMOS RF process, and its chip micrograph is shown in Fig. 14(b). It has a total die area is $570 \times 460 \mu\text{m}^2$, and a core area of 0.0085 mm^2 . For the purpose of imaging system integration, the receiver chip is firstly attached to a test board (FR4, 1.6-mm thickness). As shown in Fig. 16, the whole test board is placed on a probe station for SRX measurement. As such, the SRX can be integrated within an imaging system by



(a)



(b)

Fig. 15. Measurement results of CMOS 96-GHz SRX. (a) Gain and input S11 and (b) output voltage (V_{out}) and responsivity versus input power (P_{in}) at 95.5 GHz.

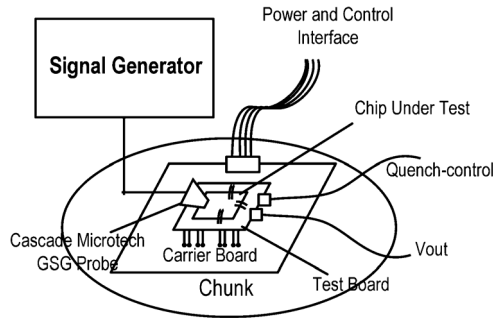
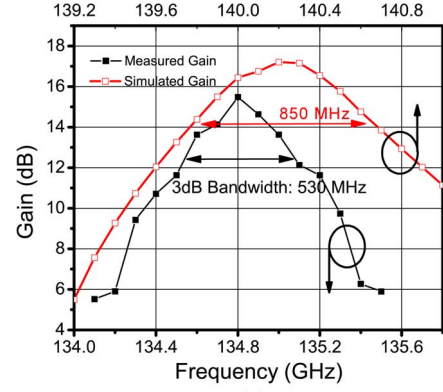


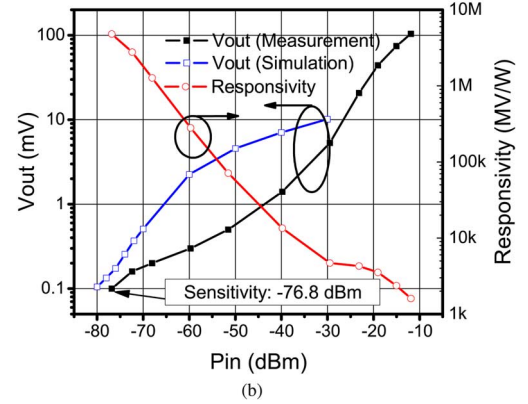
Fig. 16. Measurement setup of CMOS 135-GHz SRX with DTL-SRR.

replacing the GSG probe with bonding wires connected to an antenna. Note that the insertion loss from the bonding wires is about 1–2 dB [30]. The RF input signal is provided by a VDI D-band signal generator of which the output power is calibrated in the range from $-85 \sim -10$ dBm by an R&S FSUP signal source analyzer with a D-band waveguide harmonic mixer. A 12.5-MHz sinusoid quench-control signal is applied from a function generator (Agilent 33250a) with a voltage sweep range of 0–400 mV. Operating from a 1-V power supply, the receiver consumes 6.2 mW.

Fig. 17(a) shows the measured gain when P_{in} is -18 dBm, where the maximum gain of the proposed SRX is 15.5 dB at



(a)



(b)

Fig. 17. Measurement results of CMOS 135-GHz SRX, (a) gain, and (b) output voltage (V_{out}) and responsivity versus input power (P_{in}) at 134.8 GHz.

134.8 GHz and the 3-dB bandwidth is 530 MHz. The measured gain is also quite close to the post-layout simulation result, but the center frequency of measurement results is 5 GHz lower than that from simulation, which is probably due to the inaccurate transistor model above 100 GHz. Fig. 17(b) shows normalized V_{out} against P_{in} as well as the responsivity. The receiver sensitivity (S) is observed as -76.8 dBm at 134.8 GHz, which is 3.2 dB higher than the simulation result. The measured maximum responsivity is 4.82 MV/W. The calculated NEP values are 0.9 and 0.34 fW/ $\sqrt{\text{Hz}}$ for measurement and simulation results, respectively. In addition, the NF is found to be 9.7 dB by (10) at 134.8 GHz at room temperature of 290 K. A near linear relationship between V_{out} and P_{in} is observed when the input power is below -40 dBm, which can be utilized in post-data processing to generate millimeter-wave images.

C. Comparison and Discussion

The performance of the measurement results of the proposed SRXs is summarized in Table I as well as the previous state-of-the-art receiver designs. Compared to the direct conversion receiver [31], the SRXs have a 16–22 dB better sensitivity due to a narrower receiver bandwidth. Compared to the traditional SRX designs with the LC-tank resonator [8], [13], the proposed SRXs are showing 30%–50% reduced NEP, 2.8–4 dB better sensitivity, and 60% area reduction. Compared to the DTL-CSRR based SRX, the DTL-SRR based SRX has 40% smaller core area, which makes it more suitable for the portable millimeter-wave imaging with a large sensor array.

TABLE I
PERFORMANCE COMPARISON OF STATE-OF-THE-ART
RECEIVERS FOR IMAGING APPLICATION

Parameters	[8]	[13]	[31]	DTL-CSRR	DTL-SRR
Topology	SRX	SRX	DC	SRX	SRX
Resonator Type	LC-tank	LC-tank	-	TL-CSRR	TL-SRR
Technology Node	65 nm CMOS	65 nm CMOS	0.18 μm BiCMOS	65 nm CMOS	65 nm CMOS
f_{osc} (GHz)	144	183	103	95.5	135
Power (mW)	2.5	13.5	225	2.8	6.2
Sensitivity (dBm)	-74	-72.5	-56	-78	-76.8
Bandwidth (GHz)	0.94	1.4	20	0.56	0.53
NF (dB)	10.2	9.9	15	8.5	9.7
NEP ($\text{fW}/\sqrt{\text{Hz}}$)	1.3	1.5	17.8	0.67	0.9
Core Area (mm^2)	0.021	0.013	0.75	0.014	0.0085

However, more metal layers are required to form a DTL-SRR structure, which will also increase the chip cost.

D. 135-GHz Imaging System by DTL-SRR-Based SRX

The SRX can be easily integrated with the millimeter-wave imaging system by replacing the GSG probe with bonding wires connected to an 135-GHz antenna. It is demonstrated by wires bonding from the input of the proposed 135-GHz SRX to a 2×4 antenna array with a hybrid series/parallel feeding network, as show in Fig. 18(a). The receiver and antenna must be well aligned to minimize the connection loss. The entire millimeter-wave imaging setup is also shown in Fig. 18(b). The 135-GHz radiation from a VDI source (0 dBm) is received by proposed SRX after propagating through the objects under test, which is held by an X - Y moving stage (STANDA) placed in the middle. Generally, the frequency tuning range (FTR) of the source needs to cover the variation of the SRX operation frequency at advanced CMOS process nodes. Moreover, the tuning step size has to be sufficiently small to enable an accurate matching to the operation frequency of the SRX. Although a substantial portion of the object is illuminated due to the divergent beam from the source antenna, only the power propagating to the direction of receiver is detected. As such, a high-resolution image can be obtained without a focus lens. The resulting V_{out} at each X - Y stage position is recorded into a 2-D matrix, which can be plotted in a color image by MATLAB with a JET color map.

Fig. 19 shows the imaging results by the proposed CMOS millimeter-wave imaging system. Fig. 19(a) demonstrates the detection of a knife, perfume, and coin inside a handbag. These items can be clearly identified in the image because different material types like metal, plastic, and liquid have different absorption and reflection properties to the millimeter-wave radiation. Fig. 19(b) shows that one can differentiate between a moisturized Panadol pill and a dry one. Due to the strong water absorption at millimeter-wave frequencies, a moisturized Panadol has higher absorbtion than the dry one. The imaging system can

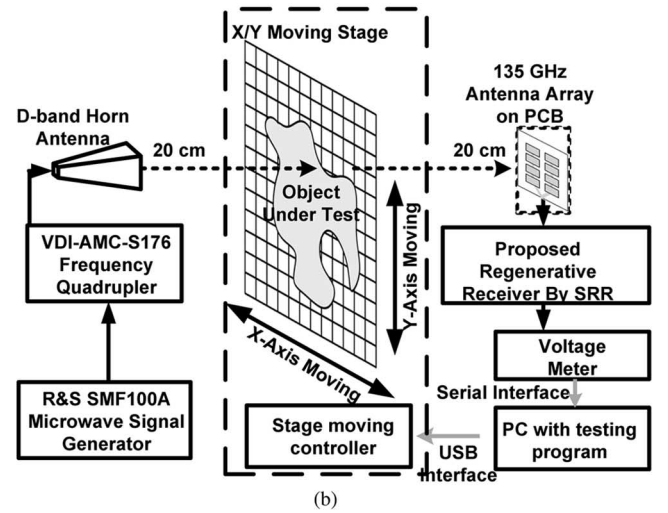
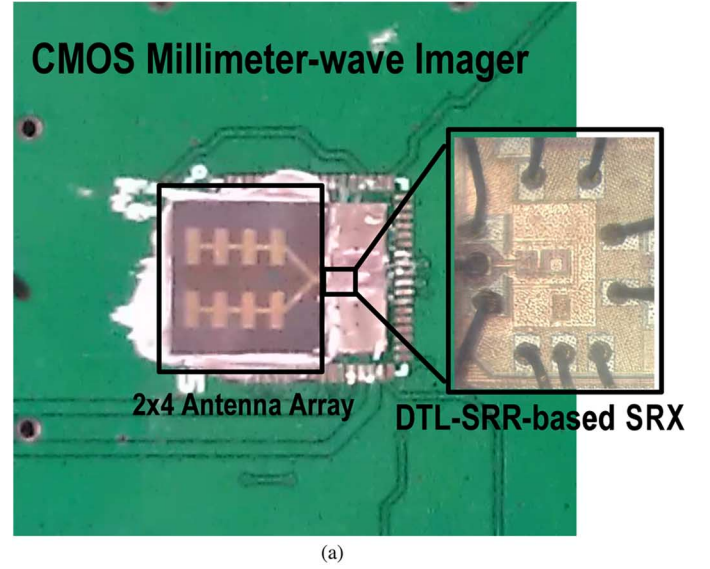


Fig. 18. (a) Printed circuit board (PCB) integration of CMOS 135-GHz SRX with antenna. (b) Millimeter-wave imaging measurement setup with the proposed receiver chip integrated on PCB and object under test fixed on an X - Y moving stage.

also be applied in transmission analysis to characterize the material in the propagation path. Fig. 19(c) shows the imaging of various types of eaten oil including sunflower, olive, fresh soybean, and soybean that has been used once. Note that four types of oil samples are held by petri dishes with the same inner diameter of 35 mm, in which the oil surfaces are perpendicular to the propagation path between transmitter and receiver. The thickness of each oil sample is controlled through the volume measurement of a syringe pump with an accuracy of 5% before being injected to the petri dish. The absorption ratio can be identified by comparing the received power under a different sample volume using (13) in Section II. Note that the measurement error contributed by the reflection loss can be minimized as the first interface signal reflection is calibrated. In addition, the accuracy of measurement results can be improved by increasing the volume difference to generate wider transmission diversity. The calculated absorption ratio of each oil type is depicted in the box chart in Fig. 20. It is interesting to observe that the soybean oil

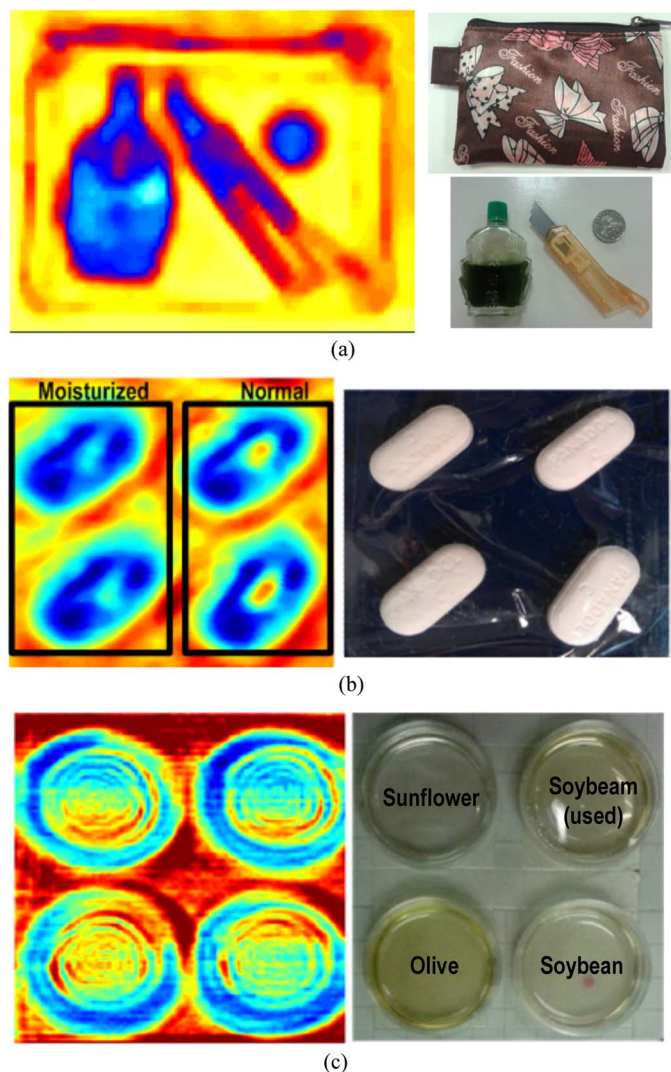


Fig. 19. Images captured by imaging system with the proposed CMOS 135-GHz SRX. (a) Knife, perfume, and coin in handbag. (b) Moisturized and normal Panadol pills. (c) Various types of oil.

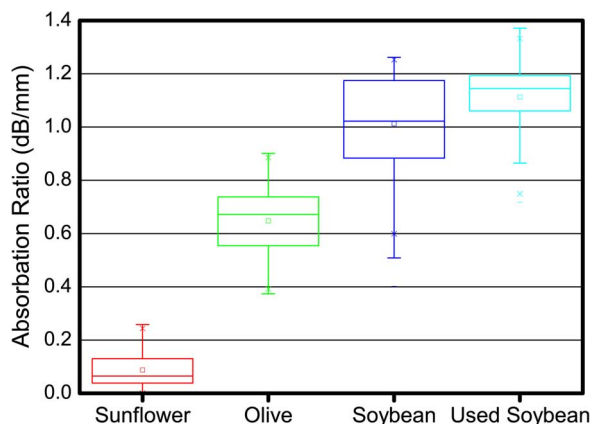


Fig. 20. Absorption ratio of various types of oil detected at 135 GHz.

that has been used once has higher absorption to the 135-GHz energy than the fresh one. With the significantly improved receiver sensitivity, the proposed CMOS millimeter-wave imager results in high contrast images and it can be further utilized in

the analysis of the moisture level, as well as the identification of particular liquid content.

VI. CONCLUSION

In this paper, a high-sensitivity SRX has been demonstrated by compact high- Q quench-controlled metamaterial resonators at 96 and 135 GHz in a 65-nm CMOS, respectively. Compared to the conventional SRX design with an LC -tank resonator at a similar frequency, the proposed SRXs have 2.8~4 dB improved sensitivity and 60% reduced area. The proposed 135-GHz SRX is integrated in a millimeter-wave imaging system with various demonstrated imaging diagnosis applications. It has great potential to be utilized for the future large-arrayed transmission-type millimeter-wave imaging system.

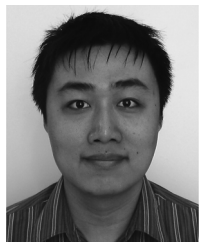
ACKNOWLEDGMENT

The authors would like to acknowledge the support of 65-nm CMOS tape-out from GlobalFoundries and MediaTek. The authors appreciate the measurement support by W.-M. Lim, VIRTUS IC Design Centre of Excellence, and Integrant Software for providing the EM simulation tool EMX.

REFERENCES

- [1] A. Nahata, A. Weling, and T. Heinz, "A wideband coherent terahertz spectroscopy system using optical rectification and electro-optic sampling," *Appl. Phys. Lett.*, vol. 69, no. 16, pp. 2321–2323, Oct. 1996.
- [2] D. Arnone, C. Ciesla, and M. Pepper, "Terahertz imaging comes into view," *Phys. World*, vol. 13, no. 4, pp. 35–40, Apr. 2000.
- [3] R. Woodward, V. Wallace, D. Arnone, E. Linfield, and M. Pepper, "Terahertz pulsed imaging of skin cancer in the time and frequency domain," *J. Biol. Phys.*, vol. 29, no. 2–3, pp. 257–261, Jun. 2003.
- [4] P. C. Ashworth, E. Pickwell-MacPherson, E. Provenzano, S. E. Pinder, A. D. Purushotham, M. Pepper, and V. P. Wallace, "Terahertz pulsed spectroscopy of freshly excised human breast cancer," *Opt. Exp.*, vol. 17, no. 15, pp. 12444–12454, Jul. 2009.
- [5] Y. Sun, M. Y. Sy, Y. X. Wang, A. T. Ahuja, Y. T. Zhang, and E. Pickwell-Macpherson, "A Promising diagnostic method: Terahertz pulsed imaging and spectroscopy," *World J. Radiol.*, vol. 3, no. 3, pp. 55–65, Mar. 2011.
- [6] W. Fei, H. Yu, Y. Shang, and K. S. Yeo, "A 2-D distributed power combining by metamaterial-based zero-phase-shifter for 60 GHz power amplifier in 65 nm CMOS," *IEEE Trans. Microw. Theory Techn.*, vol. 61, no. 1, pp. 505–516, Jan. 2013.
- [7] E. Ojefors, U. Pfeiffer, A. Lisauskas, and H. Roskos, "A 0.65 THz focal-plane array in a quarter-micron CMOS process technology," *IEEE J. Solid-State Circuits*, vol. 44, no. 7, pp. 1968–1976, Jul. 2009.
- [8] A. Tang, Z. Xu, Q. Gu, Y.-C. Wu, and M. Chang, "A 144 GHz 2.5 mW multi-stage regenerative receiver for mm-wave imaging in 65 nm CMOS," in *IEEE Radio Freq. Integr. Circuits Symp.*, Jun. 2011, pp. 1–4.
- [9] K. Sengupta and A. Hajimiri, "A 0.28 THz power-generation and beam-steering array in CMOS based on distributed active radiators," *IEEE J. Solid-State Circuits*, vol. 47, no. 12, pp. 3013–3031, Dec. 2012.
- [10] R. Han, Y. Zhang, Y. Kim, D. Y. Kim, H. Shichijo, E. Afshari, and O. Kenneth, "280 GHz and 860 GHz image sensors using Schottky-barrier diodes in 0.13 μ m digital CMOS," in *IEEE Int. Solid-State Circuits Conf.*, Feb. 2012, pp. 254–256.
- [11] B. Khamaisi, S. Jameson, and E. Socher, "A 210–227 GHz transmitter with integrated on-chip antenna in 90 nm CMOS technology," *IEEE Trans. Terahertz Sci. Technol.*, vol. 3, no. 2, pp. 141–150, Mar. 2013.
- [12] L.-H. Li, F.-L. Lin, and H.-R. Chuang, "Complete RF-system analysis of direct conversion receiver (DCR) for 802.11a WLAN OFDM system," *IEEE Trans. Veh. Technol.*, vol. 56, no. 4, pp. 1696–1703, Jul. 2007.
- [13] A. Tang and M.-C. Chang, "183GHz 13.5 mW/pixel CMOS regenerative receiver for mm-wave imaging applications," in *IEEE Int. Solid-State Circuits Conf.*, Feb. 2011, pp. 296–298.

- [14] D. Kim, J. Kim, J.-O. Plouchart, C. Cho, W. Li, D. Lim, R. Trzcinski, M. Kumar, C. Norris, and D. Ahlgren, "A 70 GHz manufacturable complementary LC-VCO with 6.14 GHz tuning range in 65 nm SOI CMOS," in *IEEE Int. Solid-State Circuits Conf.*, Feb. 2007, pp. 540–620.
- [15] S.-W. Chu and C.-K. Wang, "An 80 GHz wide tuning range push–push VCO with-boosted full-wave rectification technique in 90 nm CMOS," *IEEE Microw. Wireless Compon. Lett.*, vol. 22, no. 4, pp. 203–205, Apr. 2012.
- [16] Z. Xu, Q. Gu, Y.-C. Wu, H.-Y. Jian, and M.-C. Chang, "A 70–78 GHz integrated CMOS frequency synthesizer for-band satellite communications," *IEEE Trans. Microw. Theory Techn.*, vol. 59, no. 12, pp. 3206–3218, Dec. 2011.
- [17] D. Cai, Y. Shang, H. Yu, and J. Ren, "An 80 GHz on-chip metamaterial resonator by differential transmission line loaded with split ring resonator," *IET Electron. Lett.*, vol. 48, no. 18, pp. 1128–1130, Aug. 2012.
- [18] W. Fei, H. Yu, Y. Shang, D. Cai, and J. Ren, "A 96 GHz oscillator by high-q differential transmission line loaded with complementary split ring resonator in 65 nm CMOS," *IEEE Trans. Circuits Syst. II, Exp. Briefs*, vol. 60, no. 3, pp. 127–131, Mar. 2013.
- [19] Y. Shang, H. Yu, D. Cai, J. Ren, and K. S. Yeo, "Design of high-Q millimeter-wave oscillator by differential transmission line loaded with metamaterial resonator in 65 nm CMOS," *IEEE Trans. Microw. Theory Techn.*, vol. 61, no. 5, pp. 1892–1902, May 2013.
- [20] J. R. Whitehead, *Super-Regenerative Receivers*, 1st ed. Cambridge, U.K.: Cambridge Univ. Press, 1950.
- [21] F. Moncunill-Geniz, P. Pala-Schonwalder, and O. Mas-Casals, "A generic approach to the theory of superregenerative reception," *IEEE Trans. Circuits Syst. I, Reg. Papers*, vol. 52, no. 1, pp. 54–70, Jan. 2005.
- [22] J. Bohorquez, A. Chandrakasan, and J. Dawson, "Frequency-domain analysis of super-regenerative amplifiers," *IEEE Trans. Microw. Theory Techn.*, vol. 57, no. 12, pp. 2882–2894, Dec. 2009.
- [23] M. C. Wanke, M. A. Mangan, and R. J. Foltynowicz, "Atmospheric propagation of THz radiation," OSTI, Oak Ridge, TN, USA, Nov. 2005.
- [24] T. Schneider, A. Wiatrek, S. Preussler, M. Grigat, and R.-P. Braun, "Link budget analysis for terahertz fixed wireless links," *IEEE Trans. Terahertz Sci. Technol.*, vol. 2, no. 2, pp. 250–256, Mar. 2012.
- [25] R. A. Shelby, D. R. Smith, and S. Schultz, "Experimental verification of a negative index of refraction," *Sci.*, vol. 292, no. 5514, pp. 77–79, 2001.
- [26] F. Falcone, T. Lopetegi, J. Baena, R. Marques, F. Martin, and M. Sorolla, "Effective negative ϵ stopband microstrip lines based on complementary split ring resonators," *IEEE Microw. Wireless Compon. Lett.*, vol. 14, no. 6, pp. 280–282, Jun. 2004.
- [27] A. Lai, T. Itoh, and C. Caloz, "Composite right/left-handed transmission line metamaterials," *IEEE Microw. Mag.*, vol. 5, no. 3, pp. 34–50, Sep. 2004.
- [28] Y. Shang, H. Fu, H. Yu, and J. Ren, "A-78 dBm sensitivity super-regenerative receiver at 96 GHz with quench-controlled metamaterial oscillator in 65 nm CMOS," in *IEEE Radio Freq. Integr. Circuits Symp.*, Jun. 2013, pp. 447–450.
- [29] D. R. Smith, D. C. Vier, T. Koschny, and C. M. Soukoulis, "Electromagnetic parameter retrieval from inhomogeneous metamaterials," *Phys. Rev. E, Stat. Phys. Plasmas Fluids Relat. Interdiscip. Top.*, vol. 71, no. 3, Mar. 2005, Art. ID 036617.
- [30] J. Li, Y.-Z. Xiong, S. Hu, W.-L. Goh, D. Hou, and W. Wu, "Performance analyse on millimetre-wave bonding-wire interconnection," in *IEEE Electr. Des. Adv. Packag. Syst. Symp.*, Dec. 2010, pp. 1–4.
- [31] F. Caster, L. Gilreath, S. Pan, Z. Wang, F. Capolino, and P. Heydari, "A 93-to-113 GHz BiCMOS 9-element imaging array receiver utilizing spatial-overlapping pixels with wideband phase and amplitude control," in *IEEE Int. Solid-State Circuits Conf.*, Feb. 2013, pp. 144–145.



Yang Shang (S'11) received the B.S. and M.S. degree in electrical and electronic engineering from Nanyang Technological University, Singapore, in 2005 and 2009, respectively, and is currently working toward the Ph.D. degree with the School of Electrical and Electronics Engineering, Nanyang Technological University.

His research interests are terahertz on-chip device modeling and phase-arrayed transceivers design for both imaging and spectroscopy applications.



Yuan Liang received the B.S. degree in microelectronics from Xidian University, Xi'an, China, in 2012.

He then joined the School of Electrical and Electronic Engineering, Nanyang Technological University (NTU), Singapore. His research interests include integrated-circuit design.



Hao Yu (M'06–SM'13) received the B.S. degree from Fudan University, Shanghai, China, and Ph.D. degree in integrated circuit and embedded computing from the University of California at Los Angeles (UCLA), Los Angeles, CA, USA.

He was a Senior Research Staff Member with Berkeley Design Automation. Since October 2009, he has been an Assistant Professor with the School of Electrical and Electronic Engineering, Nanyang Technological University, Singapore. He is the Area Director of the VIRTUS Integrated Circuit (IC)

Design Center of Excellence. He has authored or coauthored 135 top-tier peer-reviewed publications and two books. His current research interests include CMOS emerging technologies such CMOS terahertz electronics and 3-D ICs.

Dr. Yu is an associate editor and a Technical Program Committee member for a number of the IEEE/ACM journals and conferences. He was a recipient of the Best Paper Award of the 2010 ACM-TODAES, the Best Paper Award nominations of DAC (2006), ICCAD (2006), and ASP-DAC (2012), the Best Student Paper Competition Finalist (Advisor) of SiRF (2013), and the Inventor Award of the Semiconductor Research Cooperation (2008).



Sanming Hu (S'07–M'12–SM'14) received the B.Eng. degree from the Nanjing University of Posts and Telecommunications, Nanjing, China, in 2004, and the Ph.D. degree (under the joint master–doctorate program) from Southeast University, Nanjing, China, in 2009.

From 2006 to 2009, he was with Nanyang Technological University, Singapore, where he began and completed his doctoral research. From 2009 to 2013, he was with the Institute of Microelectronics, Agency for Science, Technology and Research (A*STAR), Singapore, as a Senior Research Engineer, a Scientist I, and then a Scientist II. He is currently with the Institute of Microwave Techniques, University of Ulm, Ulm, Germany, as a Humboldt Research Fellow. He has coauthored approximately 50 refereed papers. His current research interests include millimeter-wave/terahertz integrated circuits with antennas, 3-D integrated circuits, through-silicon vias, and graphene.

Dr. Hu has been a guest editor for the *International Journal of Antennas and Propagation* (2014). He has also served as a reviewer for several international journals and a session chair or member of the Technical Program Committee for several international conferences. He was the corecipient (as lead author) of the Best Paper Award of the IEEE TRANSACTION ON COMPONENTS, PACKAGING, AND MANUFACTURING TECHNOLOGY (2012) and the Bronze Award from the 1st Chip Design Competition held in conjunction with the 13th International Symposium on Integrated Circuits (2011). He was also the recipient of a Research Fellowship of the Alexander von Humboldt Foundation, Germany (2013).



Xiaojun Bi received the B.S. and M.S. degrees from the Huazhong University of Science and Technology (HUST), Wuhan, China, in 2005 and 2007, respectively, and the Ph.D. degree from the National University of Singapore (NUS), Singapore in 2013.

Since April 2013, he has been a Research Scientist with the Institute of Microelectronics (IME), Agency for Science, Technology, and Research (A*STAR), Singapore. From 2007 to 2008, he was a Research Associate with the Institute of Microelectronics, Chinese Academy of Sciences (IMECAS), Beijing,

China. From 2009 to 2013, he was a Ph.D. Research Scholar with NUS and IME, A*STAR. His current research interests include RF/millimeter-wave (MMW) integrated-circuit design with a focus on high-speed optical systems, MMW imaging systems, software-defined radio systems, and gigabit/second wireless communication systems.

Dr. Bi is a reviewer for the IEEE TRANSACTIONS ON MICROWAVE THEORY AND TECHNIQUES. He was a recipient of the Best Student Paper Award of the 2010 IEEE International Conference on Microwave and Millimeter-wave Technology (ICMMT), Chengdu, China. He was a Student Paper finalist of the 2013 IEEE Microwave Theory and Techniques Society (IEEE MTT-S) International Microwave Symposium (IMS), Seattle, WA, USA.



Muthukumaraswamy Annamalai Arasu received the Bachelor's degree in electronics and communication engineering from the National Institute of Technology, Tiruchirappalli, India, in 1992.

From 1993 to 2000, he was with the Centre for Development of Telematics, Delhi, India, where he designed discrete RF circuits for VSATs. From 2000 to 2003, he was with Wipro Technologies, Bangalore, India, where he designed analog/RF integrated circuits (RFICs). From 2003 to 2004, he was with the Intel Corporation, Bangalore, India, where he de-

signed RF transmitters on CMOS for ultra-wideband (UWB). In 2004, he joined the Institute of Microelectronics (IME), Singapore, as an RFIC Designer and has led CMOS RFIC transceiver development for multiband orthogonal frequency-division multiplexing (MB-OFDM) and pulse-based UWB, Ku-band low-noise block downconverter (LNB), and, high-temperature electronics. He is currently a Technical Manager with the Integrated Circuits and Systems Laboratory, IME. He has authored/coauthored over ten international conference publications in the area of RF/analog IC design for UWB application.